

Efficient Manipulation of Magnetic Domain Wall by Dual Spin-Orbit Torque in Synthetic Antiferromagnets

Hiroto Masuda, Yuta Yamane, Takaaki Dohi, Takumi Yamazaki, Rajkumar Modak, Ken-ichi Uchida, Jun'ichi Ieda, Mathias Kläui, Koki Takanashi, and Takeshi Seki*

Current-induced domain-wall motion (CIDWM) in a synthetic antiferromagnet is a key phenomenon for developing potential high-density-packed magnetic domain-wall memory with fast operation. Here, CIDWM is reported in the antiferromagnetically-coupled two Co layers through the Ir interlayer sandwiched by the two Pt layers: Pt/Co/Ir/Co/Pt. The top and bottom Pt layers play a role for generating the spin current coming from the spin Hall effect, which gives rise to the dual spin-orbit torque (SOT) acting on the perpendicular magnetizations of the Co layers. Although a simple argument would predict that SOTs from top and bottom Pt layers cancel each other out, the dual SOT nucleates a reversed magnetic domain and drives the CIDWM effectively at current density of the order of 10^{11} A m⁻². This study also examines the effect of antisymmetric interlayer exchange coupling (AIEC) on CIDWM. A positive correlation between the magnitude of AIEC and the domain wall velocity is found, whereas the current density required for nucleating the reversed domain shows a negative correlation with the magnitude of AIEC. These facts suggest that the existence of AIEC improves the performance of CIDWM. The present results provide a new avenue to design SOT domain wall devices based on a synthetic antiferromagnet.

1. Introduction

Artificial magnetic systems with an antiferromagnetic alignment of the layers, which exploit the interlayer exchange coupling (IEC) in magnetic multilayers, are a treasure trove of functionalities for spintronics applications.^[1-4] The ferromagnetic and nonmagnetic layers in a nanoscale heterostructure can each play a different role, making the total system highly functional. For example, two ferromagnetic layers such as Co separated by a nonmagnetic layer such as Cu, Ru, or Ir exhibit an antiferromagnetic alignment due to a long-range IEC, and the magnitude of IEC, i.e., the strength of the antiferromagnetic coupling, can be tuned by varying the layer thicknesses.^[5-7] Such a controllability of antiferromagnetic properties is a feature that is not found in bulk antiferromagnets. A recent research trend in spintronics, aiming to utilize the characteristics of antiferromagnetic materials such as the low

H. Masuda, T. Yamazaki, K. Takanashi, T. Seki
Institute for Materials Research
Tohoku University
Sendai 980-8577, Japan
E-mail: takeshi.seki@tohoku.ac.jp

Y. Yamane
Frontier Research Institute for Interdisciplinary Sciences
Tohoku University
Sendai 980-8578, Japan
Y. Yamane, T. Dohi
Research Institute of Electrical Communication
Tohoku University
Sendai 980-8577, Japan

T. Dohi, M. Kläui
Institut für Physik
Johannes Gutenberg-Universität Mainz
Staudingerweg 7, 55128 Mainz, Germany

R. Modak, K.-ichi Uchida
Research Center for Magnetic and Spintronic Materials
National Institute for Materials Science
Tsukuba 305-0047, Japan

R. Modak, K.-ichi Uchida
Department of Advanced Materials Science, Graduate School of Frontier Sciences

The University of Tokyo
Kashiwa 277-8561, Japan

J. Ieda, K. Takanashi
Advanced Science Research Center
Japan Atomic Energy Agency
Tokai 319-1195, Japan

T. Seki
Center for Science and Innovation in Spintronics
Tohoku University
Sendai 980-8577, Japan

T. Seki
International Center for Synchrotron Radiation Innovation Smart
Tohoku University
Sendai 980-8577, Japan

 The ORCID identification number(s) for the author(s) of this article can be found under <https://doi.org/10.1002/advs.202514598>

© 2025 The Author(s). Advanced Science published by Wiley-VCH GmbH. This is an open access article under the terms of the [Creative Commons Attribution](#) License, which permits use, distribution and reproduction in any medium, provided the original work is properly cited.

DOI: 10.1002/advs.202514598

magnetic susceptibility, lack of the magnetic stray field, and high antiferromagnetic resonance frequencies, is called antiferromagnetic spintronics.^[8] The antiferromagnetic structures artificially formed in magnetic multilayers are a suitable platform for systematic study of the antiferromagnetic spintronics thanks to the controllability of their antiferromagnetic properties as mentioned above. Also, perpendicular magnetic anisotropy can be induced at the interfaces in a multilayer, which realizes a perpendicularly-magnetized synthetic antiferromagnet. In addition, the broken inversion symmetry at the interfaces gives rise to the interfacial Dzyaloshinskii-Moriya interaction, leading to formation of topological magnetic structures such as a skyrmion.^[9] Particularly, the antiferromagnetic skyrmion observed in an IEC multilayer^[10–13] is of interest due to the drastically changed spin dynamics resulting from the antiferromagnetic coupling of the layers. The synthetic antiferromagnets are also useful for developing high-performance spintronic devices,^[14–17] particularly based on domain walls (DWs). A previous study demonstrated a fast current-induced domain-wall motion (CIDWM) in a synthetic antiferromagnet Pt/(Co/Ni)/Ru/(Co/Ni).^[17] They exploited the exchange coupling torque as well as the spin orbit torque (SOT) induced by the spin Hall effect (SHE) in Pt.^[18]

Our previous study^[19] realized a current-induced magnetization switching in Pt/Co/Ir/Co/Pt multilayers. The two Co layers were perpendicularly magnetized and either antiferromagnetically or ferromagnetically coupled through the Ir interlayer, depending on the Ir layer thickness. The dual SOT originating from the top and bottom Pt layers acts on the magnetizations in the two Co layers. Through magnetic domain observation of the SOT switching, we found that the antiferromagnetic alignment is favorable for stable and efficient SOT-switching operations.

Apart from the SOT-related phenomena, an antisymmetric IEC (AIEC) between the two ferromagnetic layers was observed in Pt/Co/Ir/Co/Pt with wedge-shaped layers.^[20] The AIEC is induced due to the broken inversion symmetry along the in-plane direction, which was first theoretically predicted,^[21] then experimentally observed.^[22,23] After the early work confirming the existence of AIEC,^[22–24] the following studies revealed the characteristics of AIEC,^[20,25–35] e.g., the relation between IEC and AIEC.^[20,25,26] The conventional, symmetric IEC energy is expressed as $J_{AF}(\mathbf{m}_A \cdot \mathbf{m}_B)$, where J_{AF} denotes the antiferromagnetic coupling strength and \mathbf{m}_A and \mathbf{m}_B are the unit vectors representing the magnetizations in the two ferromagnetic layers, A and B. On the other hand, the AIEC energy is expressed as $\mathbf{D}_{AIEC} \cdot (\mathbf{m}_A \times \mathbf{m}_B)$, where \mathbf{D}_{AIEC} is the AIEC vector determined by system symmetry. With the film normal direction along the z direction and the inversion symmetry breaking along the y direction, \mathbf{D}_{AIEC} appears along the x direction. The AIEC prefers a noncolinear alignment of \mathbf{m}_A and \mathbf{m}_B , leading to chiral magnetic configurations that can be exploited to realize artificial 3D topological magnetic structures.^[36] Microscopic mechanisms of AIEC and its applications to the spintronic devices are therefore attracting considerable attention. Several experimental studies demonstrated that the AIEC allows the field-free SOT switching thanks to the in-plane effective field originating from the AIEC field.^[28–31] However, there is no experimental elucidation how the AIEC field affects the CIDWM. Also, the behavior of DW under the dual SOT application is not a trivial issue because a simple picture of dual SOT gives the cancellation between the SOTs from top and bot-

tom spin Hall layers. Considering the complex layer stacking incorporated into the current spintronics devices, the understanding of the mechanism and process of the SOTs coming from multiple layers is remarkably important from the viewpoint of not only an academic interest but also an efficient device operation.

This paper presents a combined experimental and theoretical study on CIDWM in a perpendicularly-magnetized synthetic antiferromagnet Pt/Co/Ir/Co/Pt with AIEC. We find that the dual SOT can effectively drive DWM in the presence of in-plane field, despite the opposite polarization of the spin current injected from the top and bottom Pt layers. We find that the AIEC can reduce the current density required for DW nucleation and increase the DW velocity. The experimental observations are consistent with our numerical simulation. The present results provide a new direction to design DW devices using a synthetic antiferromagnet.

2. Experimental Results

The following layer stackings were deposited on thermally oxidized Si substrates using a magnetron sputtering at room temperature: Si-O Subs./Ta (2)/Pt (3)/Co (0.65 or t_{Co})/Ir (1.3)/Co (0.9)/Pt (3)/Ta (1) (thickness in nanometer). **Figure 1a** illustrates the central layer stacking together with the magnetization configuration of two Co layers. The 1.3 nm-thick Ir layer leads to the antiferromagnetic IEC, and the 1.3 nm thickness is the second peak position of oscillatory behavior of IEC strength as a function of the Ir interlayer thickness.^[19] Thanks to the interfaces with the Pt layers, the top and bottom Co layers are perpendicularly magnetized. In order to intentionally break the in-plane spatial inversion, the bottom Co layers were designed to have a wedge shape (**Figure 1b**). In our previous study,^[20] the wedged Co layer was effective to induce the AIEC. As discussed later, although there are several sources for the AIEC except the wedge shape, implying that the AIEC field is determined by multiple contributions as we reported in another paper,^[35] we consider that the wedge shape becomes one of major sources breaking the in-plane spatial inversion. For the Co-wedged samples, t_{Co} denotes the thickness of wedged bottom Co layer, and the ranges of t_{Co} were set to be $0.6 \leq t_{Co} \leq 1.1$ nm, $0.4 \leq t_{Co} \leq 1.4$ nm, and $0.3 \leq t_{Co} \leq 1.8$ nm, which correspond to the thickness gradient ∇t_{Co} of 0.6×10^{-7} , 1.1×10^{-7} , and 1.7×10^{-7} , respectively. For the thin film without the wedged layer, the Co layer thickness was fixed at 0.65 nm, which is called non-wedged sample in this study. It is noted that out-of-plane direction is the easy magnetization direction for all t_{Co} in this study, which was confirmed by measuring the polar magneto-optical Kerr effect loops (**Figure S1**, Supporting Information).

In order to observe magnetic domain structures and characterize their domain wall motion, magneto-optical Kerr effect imaging was employed in this study. As depicted in **Figure 1c**, the observed domain image mainly reflects net magnetization, which is the same direction as the top Co magnetization because the top Co layer is thicker than the bottom Co layer. The possible magnetic structures in the domain wall, that is, Néel-type and Bloch-type domain walls are also illustrated in **Figure 1d**. Since the dual-SOT acts on the magnetic moments of Co layers under the electric current application, the effective magnetic field of damping-like (DL) SOT H_{DL-SOT} is also depicted in **Figure 1e**.

The thin films were patterned into a Hall-bar-shape (**Figure 2a**) with a 5 μm width-channel. The direction of wedge shape in the

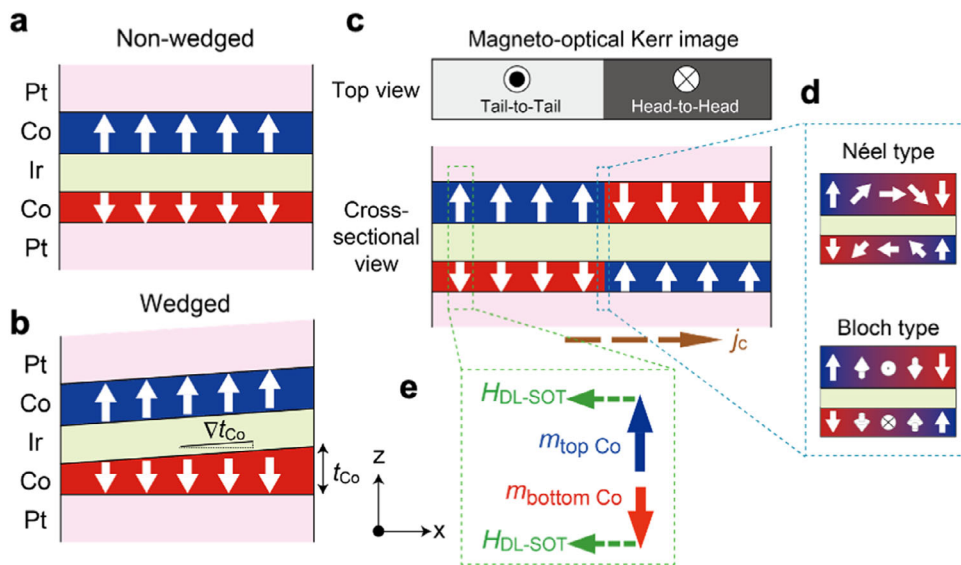


Figure 1. Schematic illustration of stacking structures together with the magnetization configuration of two Co layers for a) non-wedged sample and b) wedged sample. c) Expected magneto-optical Kerr image for a sample with tail-to-tail (light gray) and head-to-head (dark gray) magnetic domains, where the tail-to-tail domain possesses an upward net magnetization while the head-to-head domain possesses a downward net magnetization. d) Illustration of magnetic structures inside Néel-type and Bloch-type domain walls. e) Effective field of damping-like (DL) spin-orbit torque (SOT) H_{DL-SOT} acting on the top and bottom Co magnetic moments.

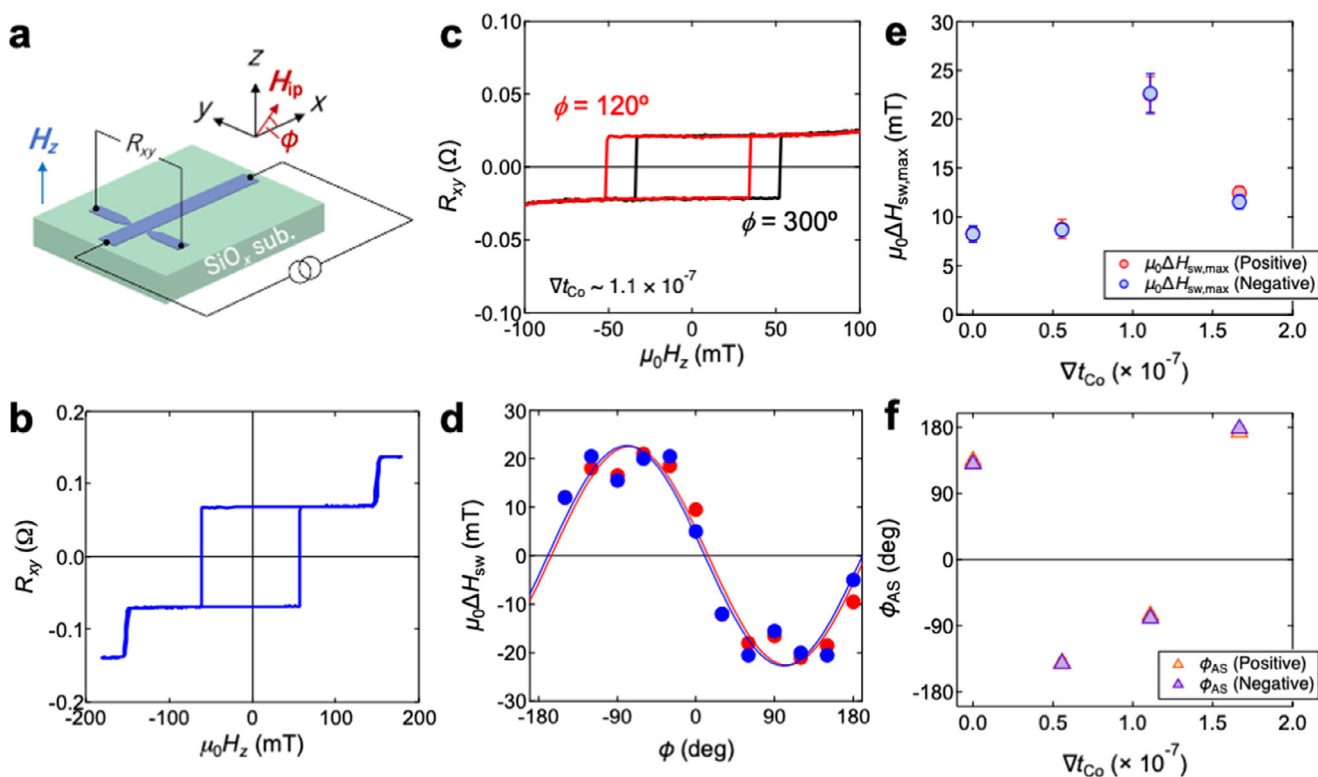


Figure 2. Characterization of symmetric interlayer exchange coupling (IEC) and antisymmetric IEC (AIEC). a) Schematic illustration of a Hall-bar device with the coordinate, where the in-plane field angle of H_{ip} is defined as the angle ϕ_{AS} from the x -axis. b) Transverse resistance R_{xy} as a function of perpendicular magnetic field H_z for the device of the non-wedged sample. c) R_{xy} curves for the device with $\nabla t_{Co} = 1.1 \times 10^{-7}$, where $\mu_0 H_{ip} = 50$ mT was applied at $\phi_{AS} = 120^\circ$ (red curve) and 300° (black curve). d) ϕ_{AS} dependence of the unidirectional shift in switching field ΔH_{sw} for the device with $\nabla t_{Co} = 1.1 \times 10^{-7}$ at $\mu_0 H_{ip} = 50$ mT. The red and blue circles denote ΔH_{sw} obtained from H_{sw} in the positive and negative field regions, respectively. The solid curves are the fitting results with cosine function. e) $\mu_0 \Delta H_{sw,max}$ and f) ϕ_{AS} as a function of ∇t_{Co} , where the red and blue marks denote the results obtained from H_{sw} in the positive and negative field regions, respectively. $\mu_0 \Delta H_{sw,max}$ and ϕ_{AS} are the fitting parameters of $\mu_0 \Delta H_{sw} = \mu_0 \Delta H_{sw,max} \cos(\phi - \phi_{AS})$, which was used in d).

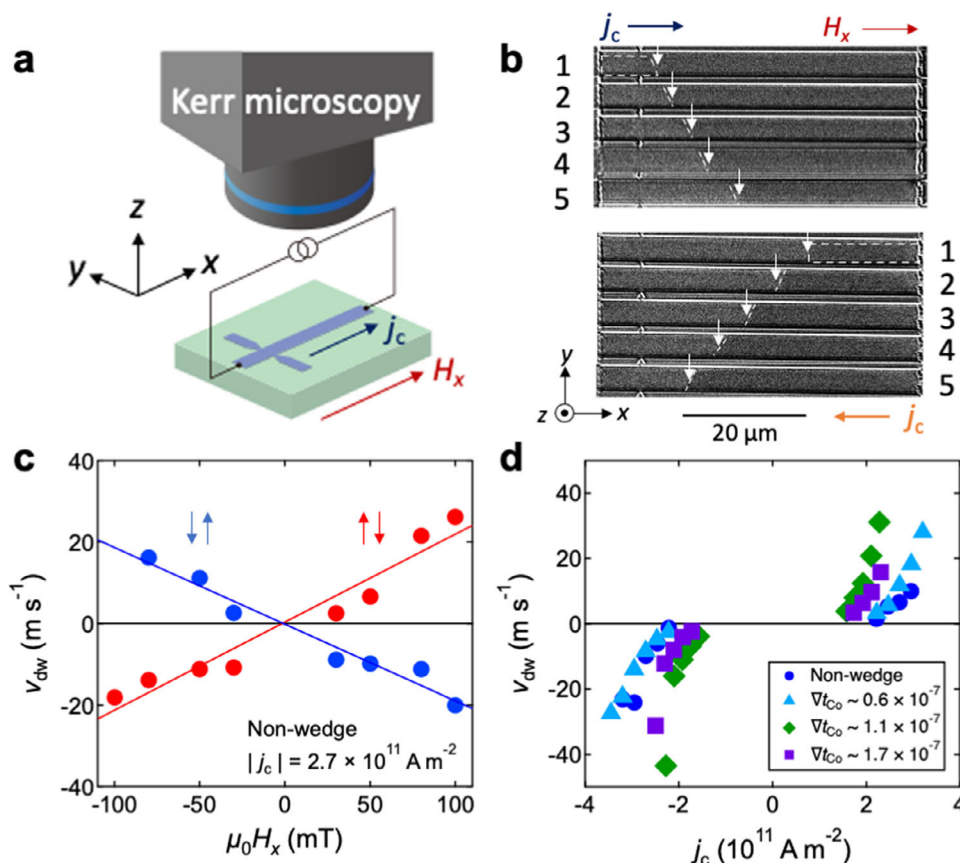


Figure 3. a) Experimental setup for the current-induced domain wall motion (CIDWM) observation using the magneto-optical Kerr microscope. b) Magneto-optical Kerr images of CIDWM for the non-wedged device at $\mu_0 H_x = 50$ mT. Top (bottom) panel shows the contrast change after applying $j_c = 2.7 \times 10^{11}$ A m $^{-2}$ with a pulse width of 500 ns in the +x (−x) direction. c) Velocity of DWM v_{dw} as a function of in-plane magnetic field H_x for the non-wedged device under the application of $j_c = 2.7 \times 10^{11}$ A m $^{-2}$. Red (blue) circles represent the data with the initial state of head-to-head (tail-to-tail) configuration. d) v_{dw} as a function of j_c for the non-wedged device and the devices with $\nabla t_{Co} = 0.6 \times 10^{-7}$, 1.1×10^{-7} , and 1.7×10^{-7} , in which $\mu_0 H_x = 50$ mT was applied.

bottom Co layer is along to the x -axis of cartesian coordinates as shown in Figure 1b. Figure 2b displays the transverse resistance R_{xy} as a function of perpendicular magnetic field H_z for the device of the non-wedged sample, where R_{xy} mainly comes from the anomalous Hall effect proportional to the perpendicular component of net magnetization of two Co layers. The two Co magnetizations are antiferromagnetically aligned at low H_z , and those are saturated ferromagnetically as H_z is increased to 200 mT. Similar to the non-wedged sample, all the samples exhibit the two Co magnetizations coupled antiferromagnetically each other due to the symmetric IEC.

In order to evaluate the magnitude of AIEC, the $R_{xy} - H_z$ curves were measured with the additional in-plane magnetic field H_{ip} . The in-plane field angle of H_{ip} is defined as the angle ϕ_{AS} from the x -axis (see Figure 2a). Figure 2c shows the $R_{xy} - H_z$ curves for the device with $\nabla t_{Co} = 1.1 \times 10^{-7}$, where $\mu_0 H_{ip} = 50$ mT was applied at $\phi_{AS} = 120^\circ$ (red curve) and 300° (black curve). In the presence of AIEC, the application of H_{ip} leads to the asymmetry in the up-to-down (UD) and down-to-up (DU) switching fields for the net magnetization due to the preferred magnetic chirality dictated by the AIEC. As a result, the unidirectional shift of $R_{xy} - H_z$ curve appears by applying H_{ip} . The magnitude of uni-

directional shift, related to the AIEC, is represented by ΔH_{sw} , which is obtained from the difference in the switching fields H_{sw} with H_{ip} at ϕ_{AS} and $\phi_{AS} + \pi$. The value of ΔH_{sw} is an indicator of the magnitude of AIEC. Figure 2d plots the ϕ_{AS} dependence of $\mu_0 \Delta H_{sw}$ for the device with $\nabla t_{Co} = 1.1 \times 10^{-7}$ at $\mu_0 H_{ip} = 50$ mT. The experimental data are fitted by $\mu_0 \Delta H_{sw} = \mu_0 \Delta H_{sw,max} \cos(\phi_{AS} - \phi_{AS})$. $\mu_0 \Delta H_{sw,max}$ represents the magnitude of AIEC, and ϕ_{AS} is the direction of AIEC, which corresponds to the in-plane direction orthogonal to \mathbf{D}_{AIEC} . μ_0 is the permeability of the vacuum. Figure 2e,f summarize $\mu_0 \Delta H_{sw,max}$ and ϕ_{AS} , respectively, as a function of ∇t_{Co} . Here, $\nabla t_{Co} = 0$ means the non-wedged sample. Originally we anticipated that the increase of ∇t_{Co} simply increases the magnitude of AIEC ($\Delta H_{sw,max}$) and the direction AIEC (ϕ_{AS}) is aligned along the wedge direction. As can be seen, however, the device with $\nabla t_{Co} = 1.1 \times 10^{-7}$ exhibits the largest $\Delta H_{sw,max}$ among the present devices. Even the non-wedged sample shows non-negligible $\Delta H_{sw,max}$. In addition, the ϕ_{AS} deviates from the expectation, that is, the x -axis ($\phi_{AS} = 0^\circ$ or 180°). These facts suggest that apart from the wedge shape in the bottom Co layer there exist other sources providing the AIEC, e.g., the thickness inhomogeneity and/or the growth-induced magnetic anisotropy. Those other contributions were suggested also in pre-

vious studies.^[19,23,35] Thus, the direction and magnitude of AIEC cannot precisely be controlled by changing the thickness gradient in this study. Nevertheless, by introducing the wedge-shaped Co layers with different thickness gradients, a series of samples exhibiting different AIEC fields allow us to examine the influence of AIEC on the CIDWM.

Figure 3a is the setup for the CIDWM observation using the magneto-optical Kerr microscope. The representative results are given in Figure 3b, which were observed for the non-wedged device. One sees that there are two gray contrasts: dark gray and light gray. The dark gray and light gray regions correspond to the magnetic domains with the head-to-head and tail-to-tail configurations, respectively, of magnetic moments between the top and bottom Co layers as depicted in Figure 1c. For the present CIDWM experiment, the reversed magnetic domain was nucleated at a certain position in the wire when the current pulse with a certain current density j_c was applied. Although this reversed domain nucleation procedure is not a precisely-controlled manner, we could successfully nucleate the reversed domain in almost the middle of wire. The domain nucleation was attributable to the switching due to the dual SOT. The positions of DWs are denoted by the white arrows. The top (bottom) panel shows the contrast change after the application of $j_c = 2.7 \times 10^{11} \text{ A m}^{-2}$ and with a pulse width of 500 ns in the $+x$ ($-x$) direction, where $\mu_0 H_x = 50 \text{ mT}$ was applied. The DW moves along the electric current direction (opposite to the direction of electron flow) with increasing the number of current pulse application. This tendency can be explained with the scenario of DWM induced by SOT.^[37–39] The spin Hall effect in the Pt and/or Ir layer generates the spin current interacting with the Co magnetizations. According to the SOT switching experiment reported previously,^[19] the major source of SOT is the spin Hall effect in the Pt layers while the spin Hall effect in the Ir interlayer is not significant. Thus, the SOT coming from the top and bottom Pt layers act on the top and bottom Co magnetizations individually.

The velocity of DWM v_{dw} is evaluated from the distance of DW movement and the duration of current pulse. Figure 3c plots v_{dw} as a function of H_x for the non-wedged device under the application of $j_c = 2.7 \times 10^{11} \text{ A m}^{-2}$. The red (blue) circles represent the data obtained for the device with the initial state of head-to-head (tail-to-tail) configuration. Considering the experimental situation depicted in Figure 1, the tail-to-tail region having the upward net magnetization (\uparrow) is created in the head-to-head region having the downward net magnetization (\downarrow) and the region with \uparrow is expanded by the CIDWM. Thus, the experiment starting from the head-to-head configuration corresponds to the CIDWM for the up-down ($\uparrow\downarrow$) DW while the tail-to-tail initial configuration leads to the down-up ($\downarrow\uparrow$) DW. Both cases exhibit the linear changes in v_{dw} against H_x , but show the opposite signs in the slopes. As can be seen, v_{dw} is almost equal to zero at $\mu_0 H_x = 0 \text{ mT}$. These experimental facts indicate that in line with previous findings the contribution of spin transfer torque within the Co layers is negligible while the SOT is the dominant source of CIDWM. The detailed discussion will be given later. Figure 3d summarizes v_{dw} as a function of j_c for the non-wedged device and the devices with $\nabla t_{Co} = 0.6 \times 10^{-7}$, 1.1×10^{-7} , and 1.7×10^{-7} , in which $\mu_0 H_x = 50 \text{ mT}$ was applied. After the nucleation of reversed domain at a certain j_c , which is defined as the nucleation current den-

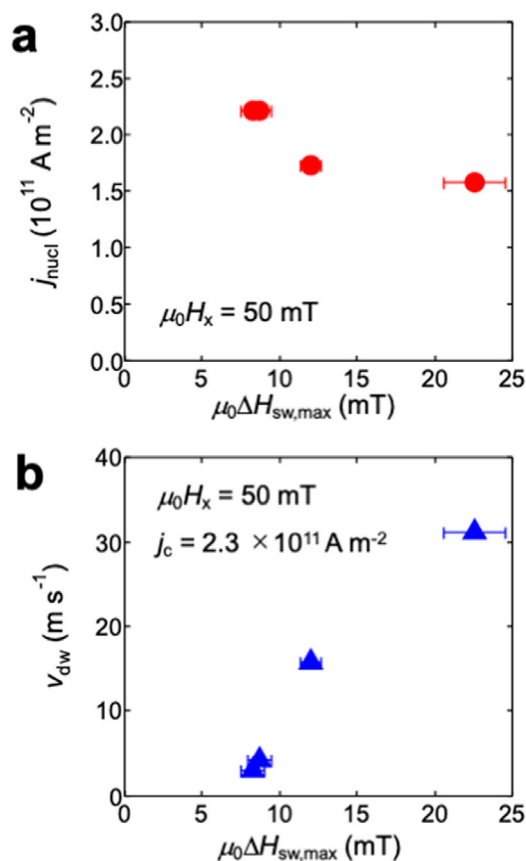


Figure 4. Effect of AIEC on nucleation current density j_{nucl} and v_{dw} for the CIDWM. a) j_{nucl} obtained at $\mu_0 H_x = 50 \text{ mT}$ as a function of $\Delta H_{sw,max}$. b) v_{dw} as a function of $\Delta H_{sw,max}$, where v_{dw} was evaluated under the application of $j_c = 2.3 \times 10^{11} \text{ A m}^{-2}$ and $\mu_0 H_x = 50 \text{ mT}$.

sity j_{nucl} , v_{dw} nonlinearly increases with increasing j_c for all the devices.

To discuss the effect of AIEC on the CIDWM, we plots the j_{nucl} obtained at $\mu_0 H_x = 50 \text{ mT}$ as a function of $\Delta H_{sw,max}$ in Figure 4a. One can see that there is a negative correlation between j_{nucl} and $\Delta H_{sw,max}$. Namely, the AIEC field promotes the nucleation of reversed domain under the dual SOT application. On the other hand, v_{dw} clearly increases with $\Delta H_{sw,max}$ as shown in Figure 4b, where v_{dw} was evaluated under the application of $j_c = 2.7 \times 10^{11} \text{ A m}^{-2}$ and $\mu_0 H_x = 50 \text{ mT}$. At this condition, the fastest v_{dw} was obtained to be 31 m s^{-1} for the device with $\nabla t_{Co} = 1.1 \times 10^{-7}$, which is one order of magnitude larger than the v_{dw} for the non-wedged device. The positive correlation between v_{dw} and $\Delta H_{sw,max}$ means that the AIEC field plays a role for the efficient CIDWM. According to the previous works,^[27,35] the oblique sputter-deposition or the selection of nonmagnetic interlayer with large spin-orbit coupling can enhance the magnitude of AIEC, leading to the further improvement of CIDWM efficiency. One may be wondering how the degree of compensation between top and bottom Co magnetizations affects v_{dw} . A previous work reported that the closely compensated state leads to the fast v_{dw} .^[17] Although the wedged bottom Co layers give a spatial change in the degree of compensation, we do not observe any relation between v_{dw} and ∇t_{Co} in the present system. In addition, one may think why even

the γ -directional AIEC field positively affects DW velocity. We consider that the present case is still far from the ideal CIDWM showing the linear correlation between v_{dw} and j_c . Rather the nucleation energy and the pinning potential for DW determine the process for CIDWM, which may be affected by the AIEC field. This is a possible explanation for the fact that the AIEC field positively affects DW velocity regardless of ϕ_{AS} .

3. Theoretical Calculation and Discussion

In order to understand the CIDWM by dual SOT, we carry out micromagnetic simulations in a synthetic antiferromagnetic nanowire with a custom-developed code. Here, we focus to elucidate the following two points: i) How the dual SOT can drive the DWM despite that a simple argument predicts that the spin injections from the top and bottom Pt layers with the opposite spin polarizations lead to a net zero effect on the magnetization dynamics. ii) How the AIEC affects the CIDWM.

We model our synthetic antiferromagnet by the following surface magnetic energy density (U),

$$U = J_{\text{AF}} \mathbf{m}_A \cdot \mathbf{m}_B + \mathbf{D}_{\text{AIEC}} \cdot (\mathbf{m}_A \times \mathbf{m}_B) + A \sum_{i=x,y,z} \left[t_A (\partial_i \mathbf{m}_A)^2 + t_B (\partial_i \mathbf{m}_B)^2 \right] - K \left[t_A (m_{A,z})^2 + t_B (m_{B,z})^2 \right] - \mu_0 M_s \mathbf{H} \cdot (t_A \mathbf{m}_A + t_B \mathbf{m}_B) \quad (1)$$

where A is the exchange stiffness, K is the perpendicular magnetic anisotropy constant, M_s is the saturation magnetization, \mathbf{H} is the external magnetic field, and $t_{\text{A(B)}}$ is the thickness of the layer A (B). The dynamics of \mathbf{m}_μ ($\mu = A, B$) are described by the coupled Landau-Lifshitz-Gilbert (LLG) equations

$$\frac{\partial \mathbf{m}_\mu}{\partial t} = -\gamma \mathbf{m}_\mu \times \mathbf{H}_\mu + \alpha \mathbf{m}_\mu \times \frac{\partial \mathbf{m}_\mu}{\partial t} - \gamma \mathbf{m}_\mu \times (\mathbf{m}_\mu \times \mathbf{H}_\mu^{\text{SOT}}) \quad (2)$$

where γ is the gyromagnetic ratio and α is the damping constant. The effective magnetic fields \mathbf{H}_μ are defined by $\mathbf{H}_\mu = -(\mu_0 M_s t_\mu)^{-1} (\delta U / \delta \mathbf{m}_\mu)$. The last term in Equation (2) describes the dual SOT, which is characterized by the effective fields

$$\mathbf{H}_\mu^{\text{SOT}} = \pm \frac{\hbar \theta_{\text{SH}}}{2e\mu_0 M_s t_\mu} j_c \mathbf{y} \quad (3)$$

with the upper (lower) sign corresponding to $\mu = A$ (B) and θ_{SH} the effective spin Hall angle.

Under the surface energy density with $\mathbf{H} = 0$, the system can accommodate a stable DW in equilibrium.^[40] We prepare a Bloch DW as the initial state, i.e., the magnetizations rotate in the yz plane in the DW region, and then examine the dynamics of the DW in the presence of current and magnetic field. We choose a Bloch DW since both the dual SOT and H_x act to stabilize a Bloch structure: The dual SOT with Equation (2) simply tries to align \mathbf{m}_A and \mathbf{m}_B along $+\mathbf{y}$ and $-\mathbf{y}$, respectively, while a Bloch structure can also reduce the Zeeman energy by allowing for the magnetizations to slightly cant toward the x direction. We assume $|\mathbf{D}_{\text{AIEC}}|$ to be sufficiently small that the influence of the AIEC on the DW structure can be ignored. The parameter set used is: M_s

$= 1.1 \times 10^6 \text{ A m}^{-1}$, $\alpha = 0.06$, $J_{\text{AF}} = 0.5 \times 10^{-3} \text{ J m}^{-2}$, $A = 1 \times 10^{-11} \text{ J m}^{-1}$, $K = 2 \times 10^5 \text{ J m}^{-3}$, $t_A = 0.9 \text{ nm}$, and $t_B = 0.65 \text{ nm}$. The values of M_s , K and J_{AF} are taken from experimental data on our Co/Ir/Co system,^[19] α from reported values for similar systems,^[41] and A from a typical value for ferromagnets.^[42] We introduce the in-plane angle $\theta_D (= \phi_{\text{AS}} - \pi/2)$ of the AIEC as $\mathbf{D}_{\text{AIEC}} = |\mathbf{D}_{\text{AIEC}}| (\cos \theta_D, \sin \theta_D, 0)$.

Figure 5a plots the calculated v_{dw} as a function of H_x under the application of $j_c = 2.7 \times 10^{11} \text{ A m}^{-2}$, where the magenta (cyan) symbols correspond to the results for the up-down (down-up) DW. Here, the AIEC is set to $|\mathbf{D}_{\text{AIEC}}| = 0.007 J_{\text{AF}}$ and $\theta_D = 45^\circ$. The calculation reproduces quantitatively well the major experimental features observed in Figure 3c: the linear dependence of v_{dw} on H_x , the sign reversal of v_{dw} between the up-down and down-up DW configurations, and no efficient CIDWM without H_x .

Figure 5b shows the j_c dependence of the calculated v_{dw} with several different $|\mathbf{D}_{\text{AIEC}}|$, where $\theta_D = 45^\circ$ and $\mu_0 H_x = 50 \text{ mT}$. v_{dw} exhibits linear dependence on j_c , and shifts vertically as $|\mathbf{D}_{\text{AIEC}}|$ varies. The nonzero v_{dw} at $j_c = 0$ is due to the combined effect of the AIEC and H_x ,^[40] as discussed in more detail below. The result in Figure 5b confirms that the dual SOT is mainly responsible for the observed DWM. The calculated CIDWM shows zero threshold current density, in contrast to the experiment (Figure 3d). The threshold in j_c for CIDWM may be attributed to the potential barrier for nucleating the reversed domains as well as pinning potentials due to impurities, which are not taken into account in the presented calculation.

Displayed in Figure 5c is the θ_D dependence of v_{dw} , with $j_c = 2.7 \times 10^{11} \text{ A m}^{-2}$ and $\mu_0 H_x = 50 \text{ mT}$. As elaborated on shortly, this θ_D dependence originates from the fact that only the γ component of \mathbf{D}_{AIEC} gives a major contribution to v_{dw} . Figure 5d plots the experimentally-observed v_{dw} as a function of θ_D . It is difficult to make a direct and systematic comparison between the experiment and calculation for technical reasons. The number of experimental data points is limited, because only a small number of devices with the desired t_{Co} can be obtained from the wedged samples. In addition, precise control of the direction and magnitude of the AIEC field remains difficult in experiments. Despite these limitations, however, our results clearly demonstrate that the DW velocity can be tuned by engineering the AIEC. A more direct comparison between the experimental and numerical results is given in Figure S2 (Supporting Information).

Here, we consider the physical mechanism underlying the DWM driven by the dual SOT. For the sake of simplicity, we assume the antiferromagnetic limit where $t_A = t_B$ and J_{AF} is by far the most dominant energy scale in U . Starting from the coupled LLG equations (2), we rewrite them in terms of the Néel vector $\mathbf{n} = \frac{\mathbf{m}_A - \mathbf{m}_B}{2}$ and the canting moment $\mathbf{m} = \frac{\mathbf{m}_A + \mathbf{m}_B}{2}$, where $|\mathbf{m}| \ll 1$ because of the strong antiferromagnetic exchange coupling. Following the procedure given in^[40] but now with the dual SOT included, it can be shown that \mathbf{m} is expressed as a function of \mathbf{n} : In a static state,

$$\mathbf{m} = \frac{1}{H_{\text{IEC}}} \mathbf{n} \times (-\mathbf{n} \times \mathbf{H} + \mathbf{H}_{\text{AIEC}} + \Delta \mathbf{H}^{\text{SOT}}) \quad (4)$$

where $\Delta \mathbf{H}^{\text{SOT}} = \mathbf{H}_A^{\text{SOT}} - \mathbf{H}_B^{\text{SOT}}$, and H_{IEC} and \mathbf{H}_{AIEC} are the effective fields associated with the IEC and AIEC, respectively. The

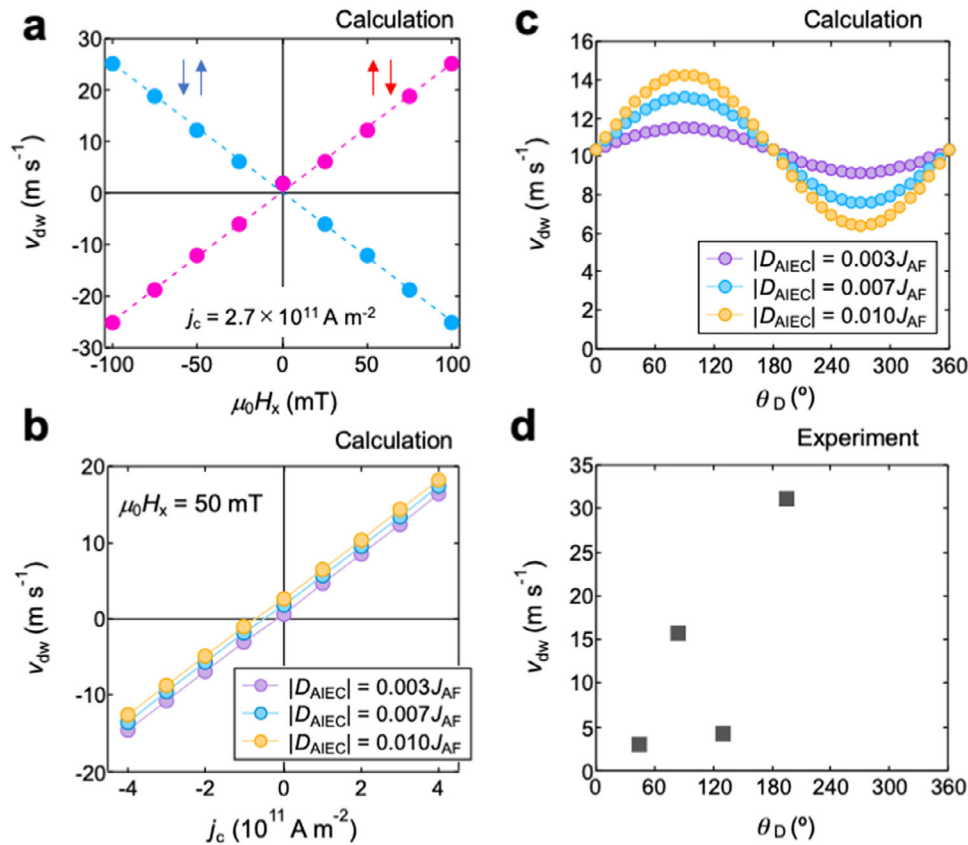


Figure 5. a) Calculated v_{dw} as a function of H_x under the application of $j_c = 2.7 \times 10^{11}$ A m⁻². The magenta (cyan) marks represent the calculated values for the up-down DW (down-up DW). b) Calculated v_{dw} as a function of j_c with changing D_{AIEC} , where $\mu_0 H_x$ was set to be 50 mT. c) Calculated v_{dw} as a function of the in-plane angle of D_{AIEC} , θ_D under the application of $j_c = 2.7 \times 10^{11}$ A m⁻², and $\mu_0 H_x = 50$ mT. d) Experimental v_{dw} as a function of θ_D under the application of $j_c = 2.3 \times 10^{11}$ A m⁻² and $\mu_0 H_x = 50$ mT.

first term in Equation (4) simply represents the field-induced canting moment. Interestingly, as indicated by the second and third terms, the AIEC and the dual SOT play the equivalent role when it comes to their contribution to \mathbf{m} . As $\mathbf{n} \approx \pm \mathbf{z}$ in each domain, the y component of $\mathbf{H}_{AIEC} + \Delta \mathbf{H}^{SOT}$ develops the x component of \mathbf{m} in the domains, which directly couples to H_x via the Zeeman interaction. The DW structure formed by \mathbf{m} following that of \mathbf{n} is therefore driven into motion by H_x , accompanied by the entire DWM. The part due to $\Delta \mathbf{H}^{SOT}$ is the CIDWM due to the dual SOT, a mechanism which has never been discussed. We note that, while the part due to \mathbf{H}_{AIEC} has been long known in the context of bulk antiferromagnets,^[40] where \mathbf{H}_{AIEC} originates rather from the crystalline symmetry, it has never been demonstrated for a DW in a synthetic thin film system. If $|D_{AIEC}|$ becomes sufficiently large, the AIEC could affect v_{dw} via stabilizing a particular DW configuration (Néel, Bloch or intermediate) depending on θ_D . While there are possible directions for further theoretical analysis, these are beyond the scope of the current work and have to be reserved for another study.

4. Conclusion

The roles of dual SOT and the AIEC for the CIDWM were experimentally and theoretically studied for the perpendicularly-

magnetized synthetic antiferromagnets using a Pt/Co/Ir/Co/Pt multilayer. The electric current application nucleates a reversed magnetic domain and shows the displacement of the domain wall existing between the head-to-head and tail-to-tail domains. From the electric current direction for CIDWM and magnetic field dependence of v_{dw} , we can conclude that the dual SOT plays the major role for CIDWM. The AIEC field contributed to the reduction of the current density required for nucleating the revised domain and leads to an increase in v_{dw} . These facts suggest that the existence of AIEC leads to the improvement of performance of CIDWM in these specially designed devices. To understand our results, we developed an appropriate theoretical model for CIDWM by dual SOT with AIEC. Our results provide a new avenue to design highly efficient SOT domain-wall devices based on a synthetic antiferromagnet.

5. Experimental Section

Thin Film Preparation and Device Fabrication: The multilayer stacks of Ta (2)/Pt (3)/Co (0.65 or t_{Co})/Ir (1.3)/Co (0.9)/Pt (3)/Ta (1) (thickness in nanometer) were deposited on a Si-O substrate using dc magnetron sputtering at room temperature with an Ar pressure of 0.4 Pa. Before deposition, the chamber was evacuated to a base pressure below 6.0×10^{-6} Pa. The area of deposited films was 9×9 mm², and t_{Co} was

continuously varied in the length of 9 mm using a linear moving shutter. The thin films were patterned into a Hall-bar-shape using electron beam lithography and Ar-ion milling. The channel width was 5 μm . The electrical contact pads of Cr (20 nm)/Au (200 nm) were fabricated using photolithography and ion-beam sputtering.

Transport Property Measurement: The transverse resistance R_{xy} was detected by applying an ac charge current of 20 μA with a frequency of 9997 Hz using a lock-in amplifier SR830. R_{xy} as a function of out-of-plane magnetic field H_z was measured with and without the additional in-plane magnetic field H_{ip} at room temperature.

Magneto-Optical Kerr Effect Imaging: The domain wall motion was visualized using a commercial Evico magnetics GmbH Kerr microscopy with an in-plane magnetic field coil. A pulse-shaped charge current with a pulse width of 500 ns was applied in a device using a function generator Agilent 33250A. The amplifier with a gain of 40 dB was connected between a function generator and a device. The pulse-shaped signal was detected using an oscilloscope Tektronix OPO7354. The external magnetic fields in the range of from 30 to 100 mT were applied during the experiments.

Supporting Information

Supporting Information is available from the Wiley Online Library or from the author.

Acknowledgements

The authors thank T. Sasaki for her help to do the film deposition by ion beam sputtering, and S. Mitani for his help for polar magneto-optical Kerr effect measurement. The device fabrication was partly carried out at the Cooperative Research and Development Center for Advanced Materials, IMR, Tohoku University. This work was supported by JSPS KAKENHI Grant-in-Aid for Scientific Research (A) (JP23H00232, JP24H00409), MEXT Initiative to Establish Next-generation Novel Integrated Circuits Centers (X-NICS) Grant Number JPJ011438, and ERATO "Magnetic Thermal Management Materials" (No. JPMJER2201) from Japan Science and Technology Agency (JST). The group in Mainz acknowledges funding by the Deutsche Forschungsgemeinschaft (DFG, German Research Foundation) – TRR 173/3 – 268565370 Spin+X (Projects B02, B13, and A01) and the European Union through the Horizon 2020 and Horizon Europe projects under Grant Agreement No. 101070290 (NIMFEIA) and EIC Pathfinder OPEN grant 101129641 (OBELIX) and the European Research Council through the Synergy Grant No. 856538 (3D MAGIC as well as the DAAD through a PPP collaborative grant between Mainz and Tohoku.

Conflict of Interest

The authors declare no conflict of interest.

Data Availability Statement

The data that support the findings of this study are available from the corresponding author upon reasonable request.

Keywords

antisymmetric interlayer exchange coupling, magnetic domain wall motion, spin orbit torque, synthetic antiferromagnet

Received: July 31, 2025

Revised: September 11, 2025

Published online: October 17, 2025

- [1] P. Grünberg, R. Schreiber, Y. Pang, M. B. Brodsky, H. Sowers, *Phys. Rev. Lett.* **1986**, 57, 2442.
- [2] M. N. Baibich, J. M. Broto, A. Fert, F. Nguyen Van Dau, F. Petroff, P. Etienne, G. Creuzet, A. Friederich, J. Chazelas, *Phys. Rev. Lett.* **1988**, 61, 2472.
- [3] G. Binasch, P. Grünberg, F. Saurenbach, W. Zinn, *Phys. Rev. B* **1989**, 39, 4828.
- [4] R. A. Duine, K.-J. Lee, S. S. P. Parkin, M. D. Stiles, *Nat. Phys.* **2018**, 14, 217.
- [5] P. Bruno, C. Chappert, *Phys. Rev. Lett.* **1991**, 67, 1602.
- [6] S. S. P. Parkin, *Phys. Rev. Lett.* **1991**, 67, 3598.
- [7] H. Masuda, T. Seki, Y.-C. Lau, T. Kubota, K. Takanashi, *Phys. Rev. B* **2020**, 101, 24413.
- [8] V. Baltz, A. Manchon, M. Tsoi, T. Moriyama, T. Ono, Y. Tserkovnyak, *Rev. Mod. Phys.* **2018**, 90, 015005.
- [9] A. Fert, V. Cros, J. Sampaio, *Nat. Nanotechnol.* **2013**, 8, 152.
- [10] T. Dohi, S. DuttaGupta, S. Fukami, H. Ohno, *Nat. Commun.* **2019**, 10, 5153.
- [11] W. Legrand, D. Maccariello, F. Ajejas, S. Collin, A. Vecchiola, K. Bouzehouane, N. Reyren, V. Cros, A. Fert, *Nat. Mater.* **2020**, 19, 34.
- [12] T. Dohi, M. Weißenhofer, N. Kerber, F. Kammerbauer, Y. Ge, K. Raab, J. Zázvorka, M.-A. Syskaki, A. Shahee, M. Ruhwedel, T. Böttcher, P. Pirro, G. Jakob, U. Nowak, M. Kläui, *Nat. Commun.* **2023**, 14, 5424.
- [13] V. T. Pham, N. Sisodia, I. D. Manici, J. Urrestarazu-Larrañaga, K. Bairagi, J. Pelloux-Prayer, R. Guedas, L. D. Buda-Prejbeanu, S. Auffret, A. Locatelli, T. O. Mentş, S. Pizzini, P. Kumar, A. Finco, V. Jacques, G. Gaudin, O. Boulle, *Science* **2024**, 384, 307.
- [14] T. Seki, H. Tomita, T. Shinjo, Y. Suzuki, *Appl. Phys. Lett.* **2010**, 97, 162508.
- [15] J.-H. Kim, J.-B. Lee, G.-G. An, S.-M. Yang, W.-S. Chung, H.-S. Park, J.-P. Hong, *Sci. Rep.* **2015**, 8, 16903.
- [16] J. Godinho, P. K. Rout, R. Salikhov, O. Hellwig, Z. Šobáň, R. M. Otxoa, K. Olejník, T. Jungwirth, J. Wunderlich, *npj Spintronics* **2024**, 2, 39.
- [17] S.-H. Yang, K.-S. Ryu, S. S. P. Parkin, *Nat. Nanotechnol.* **2015**, 10, 221.
- [18] X. Han, X. Wang, C. Wan, G. Yu, X. Lv, *Appl. Phys. Lett.* **2021**, 118, 120502.
- [19] H. Masuda, Y. Yamane, T. Seki, K. Raab, T. Dohi, R. Modak, K. Uchida, J. Ieda, M. Kläui, K. Takanashi, *Appl. Phys. Lett.* **2023**, 122, 162402.
- [20] H. Masuda, T. Seki, Y. Yamane, R. Modak, K. Uchida, J. Ieda, Y. C. Lau, S. Fukami, K. Takanashi, *Phys. Rev. Appl.* **2022**, 17, 054036.
- [21] E. Y. Vedmedenko, P. Riego, J. A. Arregi, A. Berger, *Phys. Rev. Lett.* **2019**, 122, 257202.
- [22] A. Fernández-Pacheco, E. Vedmedenko, D. Petit, R. P. Cowburn, *Nat. Mater.* **2019**, 18, 679.
- [23] D.-S. Han, K. Lee, J.-P. Hanke, Y. Mokrousov, K.-W. Kim, W. Yoo, Y. L. W. van Hees, T.-W. Kim, R. Lavrijsen, C.-Y. You, H. J. M. Swagten, M.-H. Jung, M. Kläui, *Nat. Mater.* **2019**, 18, 703.
- [24] A. Hrabec, Z. Luo, L. J. Heyderman, P. Gambardella, *Appl. Phys. Lett.* **2020**, 117, 130503.
- [25] F. S. Gao, S. Q. Liu, R. Zhang, J. H. Xia, W. Q. He, X. H. Li, X. M. Luo, C. H. Wan, G. Q. Yu, G. Su, X. F. Han, *Appl. Phys. Lett.* **2023**, 123, 192401.
- [26] S. Liang, R. Chen, Q. Cui, Y. Zhou, F. Pan, H. Yang, C. Song, *Nano Lett.* **2023**, 23, 8690.
- [27] C. O. Avci, C.-H. Lambert, G. Sala, P. Gambardella, *Phys. Rev. Lett.* **2021**, 127, 167202.
- [28] K. Wang, L. Qian, S.-C. Ying, G. Xiao, *Commun. Phys.* **2020**, 4, 10.
- [29] Y.-H. Huang, C.-C. Huang, W.-B. Liao, T.-Y. Chen, C.-F. Pai, *Phys. Rev. Appl.* **2022**, 18, 034046.
- [30] Y.-C. Li, Y.-H. Huang, C.-C. Huang, Y.-T. Liu, C.-F. Pai, *Phys. Rev. Appl.* **2023**, 20, 024032.

- [31] W. He, C. Wan, C. Zheng, Y. Wang, X. Wang, T. Ma, Y. Wang, C. Guo, X. Luo, M. E. Stebliy, G. Yu, Y. Liu, A. V. Ognev, A. S. Samardak, X. Han, *Nano Lett.* **2022**, *22*, 6857.
- [32] J. A. Arregi, P. Riego, A. Berger, E. Y. Vedmedenko, *Nat. Commun.* **2023**, *14*, 6927.
- [33] F. Kammerbauer, W.-Y. Choi, F. Freimuth, K. Lee, R. Frömter, D.-S. Han, R. Lavrijsen, H. J. M. Swagten, Y. Mokrousov, M. Kläui, *Nano Lett.* **2023**, *23*, 7070.
- [34] Y.-H. Huang, J.-H. Han, W.-B. Liao, C.-Y. Hu, Y.-T. Liu, C.-F. Pai, *Nano Lett.* **24**, 649.
- [35] T. Seki, H. Masuda, V. K. Kushwaha, T. Yamazaki, K. Ito, *J. Phys. D: Appl. Phys.* **2025**, *58*, 175002.
- [36] A. Fernández-Pacheco, R. Streubel, O. Fruchart, R. Hertel, P. Fischer, R. P. Cowburn, *Nat. Commun.* **2017**, *8*, 15756.
- [37] T. A. Moore, I. M. Miron, G. Gaudin, G. Serret, S. Auffret, B. Rodmacq, A. Schuhl, S. Pizzini, J. Vogel, M. Bonfim, *Appl. Phys. Lett.* **2008**, *93*, 262504.
- [38] P. P. J. Haazen, E. Murè, J. H. Franken, R. Lavrijsen, H. J. M. Swagten, B. Koopmans, *Nat. Mater.* **2013**, *12*, 299.
- [39] S. Emori, U. Bauer, S.-M. Ahn, E. Martinez, G. S. D. Beach, *Nat. Mater.* **2013**, *12*, 611.
- [40] V. G. Bar'yakhtar, B. A. Ivanov, M. V. Chetkin, *Sov. Phys. Usp.* **1985**, *28*, 7.
- [41] E. Barati, M. Cinal, D. M. Edwards, A. Umerski, *Phys. Rev. B* **2014**, *90*, 014420.
- [42] Y. Yamane, J. Ieda, S. Maekawa, *Appl. Phys. Lett.* **2012**, *100*, 162401.